Inorganic Chemistry

Article

pubs.acs.org/IC

Water Oxidation Catalysis by Birnessite@Iron Oxide Core–Shell Nanocomposites

Gökhan Elmaci,[†] Carolin E. Frey,[‡] Philipp Kurz,*[,‡] and Birgül Zümreoğlu-Karan*[,†]

[†]Chemistry Department, Hacettepe University, Beytepe Campus, 06800 Ankara, Turkey
[‡]Institut für Anorganische und Analytische Chemie, Albert-Ludwigs-Universität Freiburg, Albertstraße 21, 79104 Freiburg, Germany

Supporting Information

ABSTRACT: In this work, magnetic nanocomposite particles were prepared for water oxidation reactions. The studied catalysts consist of maghemite (γ-Fe_2O_3), magnetite (Fe_3O_4), and manganese ferrite ($MnFe_2O_4$) nanoparticles as cores coated in situ with birnessite-type manganese oxide shells and were characterized by X-ray diffraction, transmission electron microscopy, scanning electron microscopy, thermal, chemical, and surface analyses, and magnetic measurements. The particles were found to be of nearly spherical core–shell architectures with average diameter of 150 nm. Water oxidation catalysis was examined using Ce^{4+} as the sacrificial oxidant. All core–shell particles were found to be active water oxidation catalysts. However, the activity was found to depend on a variety of factors like the type of iron oxide core, the structure and composition of the shell, the coating characteristics, and the surface properties. Catalysts containing magnetite and manganese ferrite as core materials displayed higher catalytic activities per manganese ion (2650 or 3150 $mmol_{O_2}\ mol_{Mn}^{-1}\ h^{-1}$) or per mass than nanoiron oxides (no activity) or birnessite alone (1850 $mmol_{O_2}\ mol_{Mn}^{-1}\ h^{-1}$). This indicates synergistic effects between the MnO_x shell and the FeO_x core of the composites and proves the potential of the presented core–shell approach for further catalyst optimization. Additionally, the FeO_x cores of the particles allow magnetic recovery of the catalyst and might also be beneficial for applications in water-oxidizing anodes because the incorporation of iron might enhance the overall conductivity of the material.

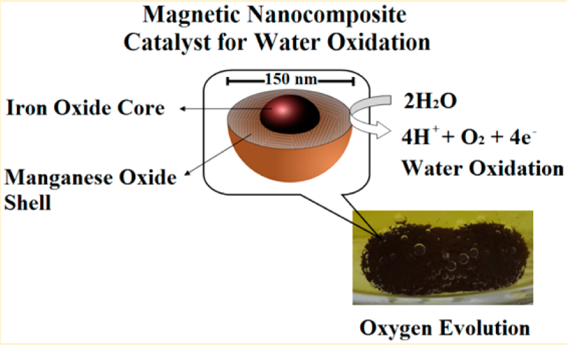

■ INTRODUCTION

As a solution to the worldwide energy demand, hydrogen holds promise as a clean energy carrier. Water splitting using renewable energy sources is a very attractive concept to generate molecular hydrogen from water as a "sustainable fuel". However, the overall water-splitting reaction requires water oxidation as one of the half-reactions, which is electrochemically difficult and thus often requires high overvoltages.[1] Many current scientific efforts therefore focus on the development of new materials for catalysis of the water oxidation process. In this field, manganese-based systems are of particular interest because they mimic the role of manganese in biological water oxidation (Photosystem II).[2] Additionally, manganese is available on a large scale because of the abundance of manganese minerals.

Various manganese compounds have been given significant attention as water oxidation catalysts in chemical, photochemical, and/or electrochemical systems.[3] Among the homogeneous systems reported, mono- and polynuclear manganese complexes showed only low catalytic rates and stabilities[4,5] but displayed better performances when adsorbed on clay or Nafion matrixes.[6−8] Compared to these molecular catalysts, manganese oxides are thermodynamically more stable. Early experiments already demonstrated that manganese(III) oxides or hydroxides are able to catalyze the oxidation of water in the presence of (photo)chemical oxidants such as Ce^{4+} or $[Ru(bpy)_3]^{3+}$ although only with low reaction rates.[9,10] Recent studies indicated that the incorporation of Ca^{2+} into the manganese oxide structure enhances the catalytic activity significantly.[11−13] X-ray diffraction and absorption studies revealed that these catalysts are materials of low crystallinity composed of layers of edge-sharing MnO_6 octahedra with interlayer Ca^{2+} ions. The manganese ions show an average oxidation state of about +3.8, and overall the materials resemble the birnessite type of manganese oxide minerals.[14,15]

Over the last years, birnessites have been closely investigated as catalysts for water oxidation.[15−17] Both performance enhancement by adding Ca^{2+} and by controlling the particle morphology seem to be of importance because nanosized $CaMnO_x$ particles proved to be more efficient catalysts than binary manganese oxides (Mn_3O_4, Mn_2O_3, and MnO_2) of similar size.[18]

In this contribution, we follow the track of morphology control and report on ∼150 nm small, magnetic MnO_x@FeO_x composite catalyst particles, which were prepared by in situ

Received: December 5, 2014
Published: February 24, 2015

© 2015 American Chemical Society

DOI: 10.1021/ic502908w
Inorg. Chem. 2015, 54, 2734−2741

coating of manganese ferrite (**MF**), magnetite (**MG**), and maghemite (**MH**) nanoparticles serving as template cores with birnessite-type manganese oxide (**B**) shells. The resulting nanocomposites show promising activities in water oxidation catalysis. Additionally, the materials' magnetic properties allow a practical recovery of the catalysts by applying an external field, and the core–shell architecture might be a useful concept to influence the electronic conductivity, a key parameter for use of the materials as electrocatalysts.

■ EXPERIMENTAL SECTION

Materials. The core materials γ-Fe_2O_3 (Sigma, nanopowder of <50 nm) and Fe_3O_4 (Aldrich, nanopowder of <50 nm) and the reagent-grade chemicals $KMnO_4$ (Merck), hydrochloric acid (HCl; Merck), $MnSO_4 \cdot H_2O$ (Merck), poly(vinylpyrrolidone) (PVP; BASF, MW 38000 Da), $Fe(NO_3)_3 \cdot 9H_2O$ (Merck), NaOAc (Merck), and ethylene glycol (Merck) were used as received.

MF was prepared following a hydrothermal synthesis procedure similar to that reported by Zhai et al.:[19] 0.70 g of $KMnO_4$, 3.13 g of $Fe(NO_3)_3 \cdot 9H_2O$, 0.90 g of PVP, and 5.97 g of NaOAc were dissolved in 60 mL of ethylene glycol and homogenized by vigorous stirring for 30 min. The resulting solution was transferred to a Teflon-lined stainless steel autoclave and maintained at 200 °C for 5 h. The black precipitate was separated by a magnet, washed with an ethylene glycol/water mixture, and then dried in an oven at ca. 70 °C. **B** was prepared by adding 0.6 g of $KMnO_4$ and 0.8 mL of concentrated HCl to 100 mL of deionized water.[20] The solution was then refluxed at 100 °C for 24 h. The product was washed with deionized water and then dried in air at 65 °C for 24 h.

General Procedure for the Synthesis of Iron Oxide–Manganese Oxide Nanocomposites. Magnetic core–birnessite shell nanocomposites were fabricated by in situ coating of iron oxide nanoparticles with **B** for which a modification of McKenzie's method was applied.[21] In a typical procedure, 0.05 g of iron oxide was sonicated for 30 min in 20 mL of deionized water. Then, 0.15 g of $KMnO_4$ and several drops of concentrated HCl were slowly added with vigorous stirring. The solution was stirred mechanically and refluxed at 100 °C for 3 h to obtain **B@MH** and **B@MG** and for 24 h to yield **B@MF** nanocomposites. The products were separated using a magnet, thoroughly washed with deionized water, and dried at 65 °C for 24 h.

Characterization. Elemental analysis for metal ions was performed using a PerkinElmer DRC II model ICP-MS spectrometer after digesting the samples (0.02 g) in a microwave with concentrated HNO_3 and HCl (4 mL each) followed by a dilution with deionized water to 50 mL. The water content was determined by thermogravimetric analysis (TGA) on a Shimadzu DTG-60H thermal analysis system at a heating rate of 10 °C min^{-1} under a nitrogen flow (100 mL min^{-1}). Powder X-ray diffraction (XRD) patterns were recorded using a Rigaku D/MAX-2200 diffractometer equipped with graphite-filtered Cu K_α radiation (λ = 1.54056 Å) from 3 to 70° (2θ) at a scanning rate of 2° min^{-1}. Fourier transform infrared (FTIR) spectra were recorded for the range 400–4000 cm^{-1} on a PerkinElmer Spectrum One spectrometer using the KBr pellet technique. The morphologies of the as-prepared samples were examined with field-emission scanning electron microscopy (FEI Quanta 200 FEG) combined with energy-dispersive X-ray spectroscopy (EDS) and high-resolution analytical transmission electron microscopy (FEI Tecnia G2 F30 instrument operating at 300 or 100 kV). The specific surface areas (Brunauer–Emmett–Teller, BET) were determined with a Monosorb Model/Quantachrome instrument. Analysis was made by a multipoint method with nitrogen gas as the adsorbent after the samples were degassed at 70 °C for 4 h. Magnetism of the products was measured at room temperature with a vibrating-sample magnetometer (Quantum Designed Physical Property Measurement System) in the magnetic field range of ±30 kOe. X-ray photoelectron spectroscopy (XPS) was carried out on a PHI VersaProbe 5000 instrument with a monochromatic 100 μm beam of Al K_α radiation as the X-ray source (15 kV) at a fixed incident angle of 45°.

Water Oxidation Catalysis Using Ce^{4+} as the Chemical Oxidant. Precisely weighed particle samples (about 5 mg each) and 685 mg (1.25 mmol) of ammonium cerium(IV) nitrate $[(NH_4)_2Ce(NO_3)_6]$ were filled into 20 mL septum vials. After the addition of 5 mL of air-saturated water, the vials were capped immediately using gastight septa and sonicated for 20 s. The reaction containers were now kept at 40 °C in a water bath, and headspace gas samples (100 μL each) were taken from the vials at 10 min intervals using a gastight syringe (Hamilton). The gas samples were injected into a PerkinElmer Clarus 480 gas chromatograph equipped with a 12 ft × $^1/_8$ in., 5 Å molecular sieve column (Restek) and a thermal conductivity detector. Six injections at 10 min intervals were carried out.

The amount of evolved oxygen was then calculated for each headspace extraction from the detected oxygen/nitrogen signal ratios. To do so, the amount of oxygen from air (corresponding to the detected nitrogen peak) was calculated and subtracted, leaving excess oxygen generated by the water oxidation reaction. For further details concerning the methodology of the water oxidation catalysis runs used here, refer to ref 13.

■ RESULTS AND DISCUSSION

Characterization of Core Materials. The core materials were characterized by powder XRD, SEM, and TEM analyses and magnetic measurements. Figure 1 illustrates the powder XRD patterns of bare iron oxide nanoparticles and birnessite shell and birnessite-coated iron oxide particles. Pattern **MH** indicates a single phase with characteristic sharp reflections at 30.2° (220), 35.7° (202), 43.4° (400), 53.9° (422), 57.4° (511), and 64.1° (440), matching the dataset JCPDS 39-1346 for γ-Fe_2O_3. The diffraction peaks at 30.1° (220), 35.6° (311), 43.3° (400), 52.5° (422), 57.2° (511), and 62.8° (440) shown for **MG** were indexed to the standard data of Fe_3O_4 (JCPDS 19-629). Pattern **MF** shows reflections at 18.3° (111), 30.2° (220), 35.5° (311), 36.9° (222), 43.1° (400), 53.5° (422), 57.0° (511), and 62.6° (440) and indicates the presence of $MnFe_2O_4$ as the main phase in accordance with the data in JCPDS 17-465.

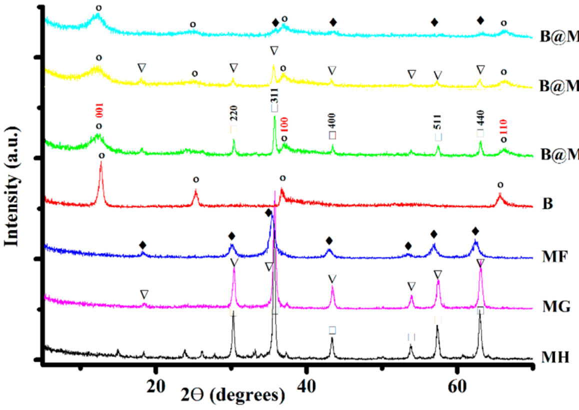

Figure 1. Experimental and theoretical powder XRD patterns (see text) of the core materials (**MH**, **MG**, and **MF**), pure birnessite (**B**), and birnessite@iron oxide composites (**B@MH**, **B@MG**, and **B@MF**).

SEM images of the core particles indicated a nearly spherical (primarily polyhedral) morphology for **MH** and **MG** (see Figures S1 and S2 in the Supporting Information, SI) and a more uniform spherical morphology for **MF** (Figure 2a). TEM images of **MH** and **MG** revealed average sizes in the range of 20–60 nm, where some of the particles were bigger because of the agglomeration of small grains (see SI). **MF** nanoparticles of

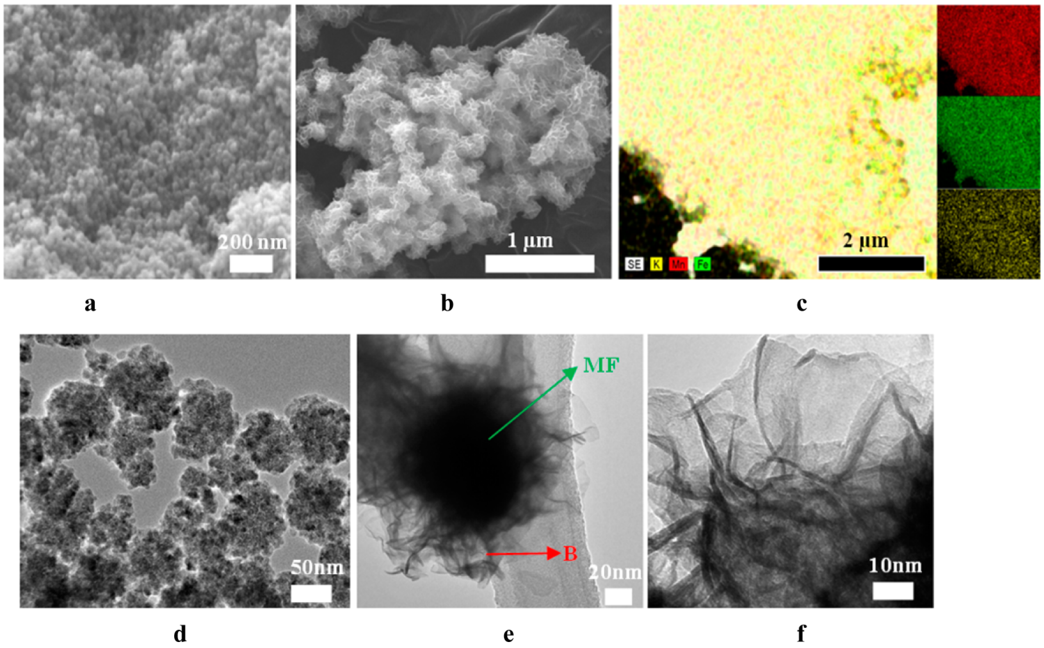

Figure 2. (a) SEM image of **MF**, (b) SEM image of **B@MF**, (c) SEM−EDS mapping of **B@MF**, (d) TEM image of **MF**, (e) TEM image of **B@MF**, and (f) magnified TEM image of **B@MF**.

50 nm size were, in fact, agglomerates of smaller (5−10 nm) particles (Figure 2d), which could well explain the observed broadening of the XRD reflections in Figure 1, pattern **MF**.

Characterization of Birnessite@Iron Oxide Nanocomposites. As described in the Experimental Section, **B** was in situ deposited on the magnetic iron oxide core. **MH**, **MG**, and **MF** nanoparticles coated by **B** were characterized by powder XRD, SEM, TEM, TGA, chemical composition (inductively coupled plasma mass spectrometry ICP-MS), and magnetic and surface area measurements. The XRD patterns of the composite particles shown in Figure 1 indicate diffraction maxima corresponding to both the **B** shell and the iron oxide core. Pattern **B** contains four well-defined diffraction peaks, (001), (002), (100), and (110), with the (001) reflection being the strongest, which is typical for the layered birnessite structure (JCPDS 80-1098). The (001) lattice plane corresponds to an interlayer distance of 7.2 Å. Distinct core and shell peaks in the XRD patterns of the composites are difficult to observe because of the Scherrer broadening of the diffractions of nanosized core and shell components compared to the corresponding patterns of plain bulk counterparts. The XRD patterns for **B@MH** and **B@MG** clearly show the characteristic reflections of both the core iron oxide phases and the birnessite shell. For **B@MF**, only the more intense of the inherently broad and weak diffractions of manganese ferrite [35.5° (311), 43.1° (400), 57.0° (511), and 62.6° (440)] are visible next to the signals of the birnessite nanocurls.

Figures 2b and S1b/S2b in the SI represent SEM images of the composites and SEM−EDS element distributions (Figures 2c and S1c/S2c in the SI), verifying homogeneous distributions of the elements (potassium, manganese, and iron) in the samples on the micrometer scale. Typical TEM images shown in Figure 2e and the SI clearly demonstrate the core−shell nature of the composites, where the rigid iron oxide particles are hierarchically decorated with curled birnessite nanosheets of ca. 5 nm thickness (Figure 2e,f). For all three iron oxide cores used here, the composite nanoparticles have similar nearly spherical morphologies with average diameters of 150 ± 20 nm, where the magnetic core of 50−60 nm size is covered with a birnessite shell of 40−50 nm thickness. The small differences in the particle shape and size also result in similar BET surface areas detected by N_2 sorption experiments. As listed in Table 2, SBET for the three different **B@FeO$_x$** composites differ only slightly, and all fit into the range of 175−225 $m^2\ g^{-1}$. Finally, the selected-area electron diffraction (SAED) patterns recorded during TEM measurements (representatively given for **B@MH** in the SI, Figure S3) include spots referring to the magnetic core as well as a couple of weak rings corresponding to the crystal planes of birnessite and are therefore in agreement with the phase assignments deduced from the XRD data discussed above.

In combination, the results of the XRD, EDS, and SAED analyses thus confirm the presence of both the desired iron and manganese oxide phases in the composite materials. Furthermore, TEM micrographs and sorption measurements clearly show that the chosen synthetic route can be successfully used to prepare the intended particle architecture: birnessite layers decorating different FeO_x cores are observed with a resulting particle diameter of the **B@FeO$_x$** composites of ∼150 nm and surface areas of ∼200 $m^2\ g^{-1}$.

The stability of the composites at elevated temperatures was examined by TGA. Figure 3 shows a comparison of the TGA curves of pure birnessite and **B@FeO$_x$** composites, where the birnessite part was in each case prepared via the same route. TGA indicates that the composites have similar thermal profiles, with a first weight loss of ∼12−18 wt % occurring between 100 and 400 °C followed by a small, but much sharper event between 500 and 600 °C. Because the iron oxides used here show only minor changes detectable by TGA under a N_2 atmosphere (see the SI, Figure S4), all events detected by thermoanalysis for the composites are manganese-related. The observed behavior is in our view concurrent with the following steps: (i) desorption of physically adsorbed and interlayer water from the birnessite material up to 500 °C; (ii) transformations

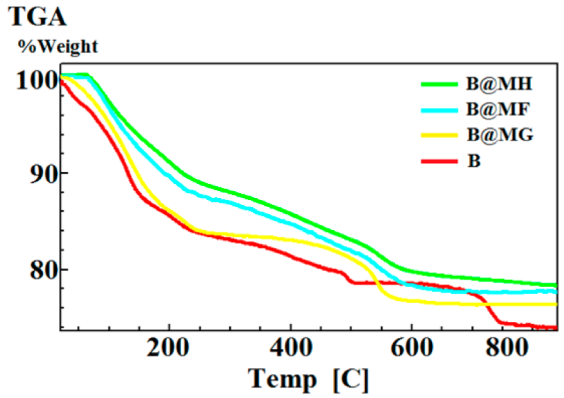

Figure 3. TGA curves of pure birnessite and the composites.

of the manganese oxide phases above 500 °C. As is visible in Figure 3 and known from previous studies on synthetic birnessites,[12,13] the removal of water takes place over a large temperature range extending up to 500 °C and therefore partly overlaps with the second step. The weight losses above 500 °C are due to the well-known release of oxygen during the conversion of "MnO_2" to manganese oxides of oxidation states <+IV.[13,22]

Together with elemental analysis data, the TGA weight loss values were used to determine the compositions of the prepared samples (Table 1). A typical birnessite has a manganese oxidation state of +3.6 to +3.8 and contains secondary cations to compensate for Mn^{4+} vacancies in the layers of MnO_6 octahedra.[14] The low potassium/manganese ratios of 0.005–0.01 found here for the composites indicate that in our cases only trace amounts of potassium have been introduced into the manganese oxide layers and the shell is most likely a birnessite containing H^+ and/or $Fe^{2+/3+}$ as additional cations. This is in marked contrast to our previous experiences concerning the preparation of different metal (M) birnessites (M = K, Mg, Ca, Sr) in alkaline solution[12,13] or also the synthesis of pure **B** as carried out here. Instead, the detected elemental composition indicates that under the synthetic conditions used here, during the in situ coatings, protons or iron cations are for some so far unknown reason preferentially bound in the interlayer space of the birnessite shell in comparison to K^+, which is also present in the reaction mixture in a significant concentration.

The water content of the composites is difficult to deduce from TGA data because the removal of physically adsorbed and structural water present in the birnessite[23] continues up to 500 °C while transformation of the birnessite structure already begins. Correlations of the total mass loss values with the proposed formulations were also difficult because of the possibility of the formation of different oxide forms of manganese. Nevertheless, we attempted to deduce tentative formulas for the different compounds **B** and **B@FeO$_x$**, which are listed in Table 1. In each case, we set the average manganese oxidation state to +3.7, as is typical for birnessites, used the potassium, iron, and manganese contents detected by ICP-MS, recorded the total mass loss values from TGA, and assumed that the manganese oxides of the shells are quantitatively converted into Mn_2O_3 once a temperature of 800 °C has been reached in the TGA experiments. As can be seen by the small differences between the found and calculated values (Table 1, numbers in brackets), this multiparameter fit seems to yield reasonable elemental compositions for the core–shell particles.

The magnetic properties of the composites were characterized by vibrating-sample magnetometry studies. The room temperature magnetization curves of the different materials were all quite similar, and as a typical example, the curve for **B@MF** is shown in Figure 4 (for additional magnetization curves, see the SI, Figures S5 and S6). The σ_s values obtained for bare core samples concur with the reported values for pure iron oxides.[24] The saturation magnetization values of the composites per sample mass were lower than those of pure core materials because the weight fraction of the magnetic core is lower than that in the bulk because of the contribution of the manganese oxide shells. However, it is still sufficiently high to allow particles to be removed fast from suspension using a magnet (Figure 5), while the particles stay suspended in water for 1 h or more if no magnetic field is applied. The observed minimal hysteresis behavior (inset in Figure 4) and saturation magnetization values given in Table 2 indicate soft ferromagnetic properties for each of the prepared composites.

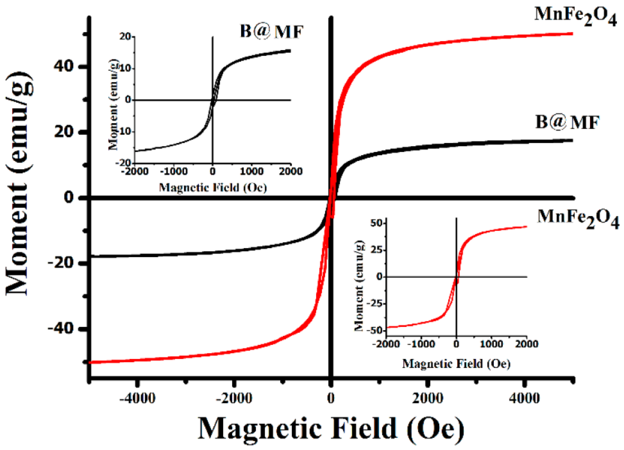

Figure 4. Room temperature magnetization curves for bare- and birnessite-coated $MnFe_2O_4$ particles.

Water Oxidation Catalysis by Birnessite@Iron Oxide Nanocomposites. To investigate the catalytic activities of the

Table 1. Chemical Compositions of the Synthetic Birnessite and the Core–Shell Particles Prepared for This Study[a]

sample	composition	K (%)	Mn (%)	Fe (%)	H_2O (%)[b]	total weight loss (%)
B	$K_{0.3}MnO_2 \cdot 1.8\ H_2O$	10.3 (10.3)	41.8 (41.3)		18 (24)	26 (28)
B@MH	$3.5\{M_{0.3}MnO_2\ \cdot 1.9H_2O\}^c@Fe_2O_3$	0.21	32.5 (32.9)	19.7 (19.1)	15 (20)	22 (25)
B@MG	$5.5\{M_{0.3}MnO_2\ \cdot 2.1H_2O\}^c@Fe_3O_4$	0.10	31.4 (32.9)	16.4 (18.3)	18 (22)	25 (27)
B@MF	$2.2\{M_{0.3}MnO_2 \cdot 3.0\ H_2O\}^c@MnFe_2O_4$	0.14	28.7 (32.5)	18.1 (20.7)	16 (22)	23 (24)

[a] The values in parentheses refer to the values calculated from the formulas proposed. [b] Calculated from the TGA-detected mass loss up to 400 °C. [c] M represents cations that are part of the birnessite structure and are needed for charge balancing, which could be M = H^+, K^+, $^{1/2}Fe^{2+}$, or $^{1/2}Mn^{2+}$.

DOI: 10.1021/ic502908w
Inorg. Chem. 2015, 54, 2734–2741

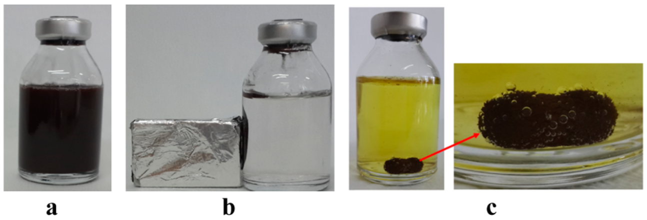

Figure 5. (a) **B@MF** suspension in water. (b) Response of the catalyst suspension to an external magnetic field. (c) Oxygen evolution after Ce^{4+} was added to the catalyst suspension, stirred by a magnetic stir bar of 2 cm length.

described birnessite–iron oxide nanocomposites, water oxidation experiments were carried out. We decided to use the chemical oxidation agent Ce^{4+}, a commonly used procedure to probe water oxidation catalysis.[11,15,25] Ce^{4+} is a strong single-electron acceptor ($E \sim +1.6$ V vs NHE) in water, and ^{18}O-isotope labeling demonstrated that such experiments indeed represent a true water oxidation process because all evolved oxygen originates from the bulk water.[26] Additionally, Ce^{4+} solutions have shown good long-term stabilities in previous studies, making it possible to screen the catalytic activity for extended time periods.[12,13]

For the water oxidation experiments, the composites were stirred at 40 °C in an aqueous solution of Ce^{4+} (250 mM) in a septum-sealed vial. The slightly elevated temperature was chosen to make comparisons with our earlier studies on water oxidation catalysis by manganese oxide possible, where the higher than ambient temperatures had been a requirement of the previously used detection system.[12,13] Birnessite powder **B**, which has been prepared in the same way as MnO_x of the shells, and also the different iron oxide materials on their own were screened as reference compounds. While the water oxidation reaction takes place, the oxygen-to-nitrogen ratio in the headspace over the suspension is monitored every 10 min via gas chromatography. Using nitrogen as an internal standard, the amount of evolved oxygen can then be calculated following a previously established procedure.[13]

In Figure 6, oxygen evolution curves obtained by this methodology are shown for four different oxide materials and first demonstrate that all three nanocomposite materials clearly are catalytically active in water oxidation and then show stable catalytic rates for at least 60 min even in the rather harsh reaction environment of "Ce^{4+}-conditions" (pH ~ 2; $E \sim +1.6$ V vs NHE). In comparison, the iron oxide nanoparticles on their own (**MH**, **MG**, and **MF**) do not show any significant catalytic activities in reactions with Ce^{4+}, and sometimes even some oxygen consumption is observed (see the SI, Figure S7, left). Furthermore, even the fastest system from the Ce^{4+} experiments (**B@MF**) does not evolve oxygen, when instead of the addition of the strong oxidation agent, it is just illuminated by visible light and no O_2 formation is detected even after hours of reaction time (see the SI, Figure S7, right). Thus, purely *photochemical* water splitting is not possible with our core–shell particles. This observation is in agreement with studies concerning photoreactions of haematite (Fe_2O_3), where water splitting into hydrogen and oxygen is also only found when an external bias voltage is used to compensate for the position of the conduction band, which is unsuitably high for proton reduction.[27]

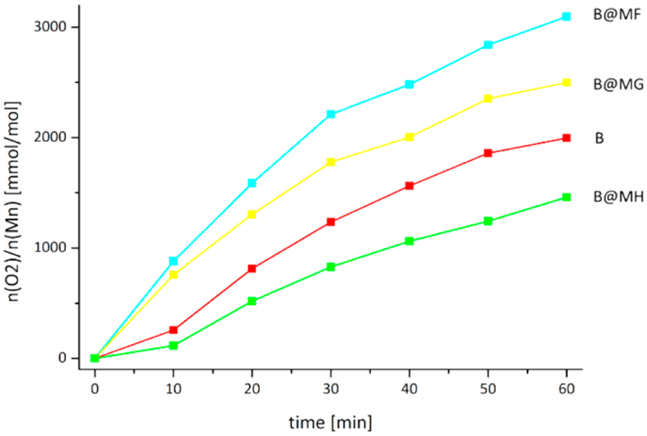

Figure 6. Oxygen evolution curves for reactions of potassium birnessite (**B**) and three types of $\mathbf{MnO_x@FeO_x}$ core–shell particles with Ce^{4+}. The amount of evolved oxygen was normalized per mole of manganese. Reaction conditions: aqueous suspensions with 1 mg of oxide mL^{-1}; $[Ce^{4+}] = 250$ mM; $T = 40$ °C. The estimated experimental error of the entire measurement procedure is ~±10%.[13]

A difficult and much discussed problem for catalysis experiments on water oxidation is the appropriate normalization method used to compare the reaction rates. Because it is nearly certain that the active site for water oxidation in these systems contains manganese ions, it has become common to calculate the amount of evolved oxygen per mole of manganese present,[13,18,25] and this has been done for the data shown in Figure 6. In such an analysis, the core–shell particles **B@MF** and **B@MG** show significantly better catalytic rates than the "standard" birnessite catalyst **B** over the entire time course of the experiments and as a consequence also in the comparison of the oxygen evolved per manganese ion after 1 h, as given in Table 2, fifth column.

To put the observed catalytic rates into perspective, Figure 7 represents a bar diagram of the averaged oxygen evolution rates found here with data for a recently studied series of potassium and calcium birnessites.[13] Experiments were run under identical conditions and are again first shown for normalization per manganese center. Within a 10% error margin, the best material found here (**B@MF**) reaches the same catalytic rate as the best

Table 2. Some Characteristics of the Prepared Composites

sample	BET surface area (m^2 g^{-1})	σ_s (emu g^{-1})[a]	core mass (% w/w)	O_2 evolution rate ($mmol_{O_2}$ mol_{Mn}^{-1} h^{-1})	O_2 evolution rate ($mmol_{O_2}$ g_{oxide}^{-1} h^{-1})	O_2 evolution rate (μmol_{O_2} m_{BET}^{-2} h^{-1})
B	25			1850	14.0	500
B@MH	175	59 (121)	27	1450	8.6	50
B@MG	205	9 (73)	25	2650	15.2	75
B@MF	210	18 (50)	43	3150	16.4	80

[a] Saturation magnetization σ_s of the composite; in parentheses, σ_s of the bare core material. **B**: birnessite. **B@MH**: birnessite coated maghemite. **B@MG**: birnessite coated magnetite. **B@MF**: birnessite-coated manganese ferrite.

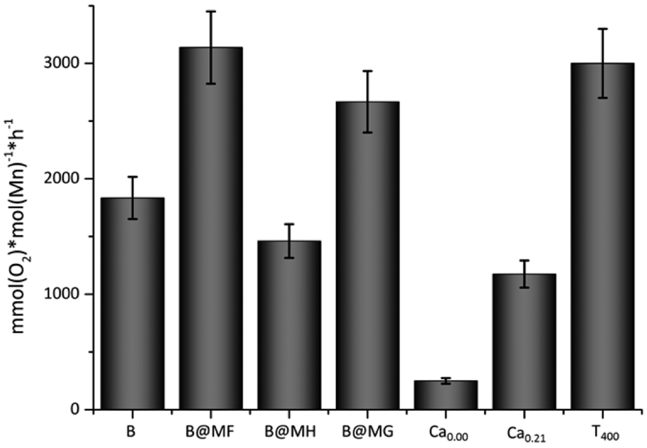

Figure 7. Comparison of the water oxidation rates for reactions of the reference birnessite **B** and the **MnO$_x$@FeO$_x$** nanocomposites of this study with synthetic potassium/calcium birnessite of a recent optimization series.[13] Normalizations per mole of manganese are shown, and the bars indicate the estimated experimental error of ∼±10%. Reaction conditions in all cases are as in Figure 6. Concerning the synthesis and properties of the catalysts **Ca$_{0.00}$**, **Ca$_{0.21}$**, and **T$_{400}$**, consult ref 13.

MnO$_x$ of the previous optimization series, a calcium containing birnessite annealed at 400 °C ("**T$_{400}$**").[13] This is very encouraging because in the present study neither calcium incorporation nor temperature treatment has been optimized (both proved to be important factors enhancing catalysis[13]), and still an oxygen evolution rate was observed for **B@MF**, which ranks among the fastest known for manganese oxides in Ce^{4+}-type experiments.

The trends concerning the catalytic activities of the **MnO$_x$@FeO$_x$** nanocomposites described so far are also very similar when the reaction rates are normalized per catalyst mass (Table 2 and Figure S8 in the SI). Again **B@MF** and **B@MG** perform very well in comparison. However, the fact that the iron oxide core contributes significantly to the mass but is most certainly not the site of the catalytic process renders **T$_{400}$**, the best catalyst of the previous study, superior to the core−shell particles in this statistic.

A third obvious manner of normalization for a heterogeneous catalytic process is calculation of the rates per catalyst surface area because the reaction is expected to take place at the interface of the material with the solution and the rates are thus expected to scale with the size of this contact area. The values for this normalization are shown in Table 2, last column, and also in the SI, Figure S9. Once more, similar trends within the three **MnO$_x$@FeO$_x$** materials can be found, and again **B@MF** and **B@MG** compete reasonably well with the synthetic potassium/calcium birnessites. An exception here is **B**, the potassium birnessite reference compound. Unlike the potassium/calcium birnessites of previous studies (prepared at pH > 12 from the reaction of Mn^{2+} with MnO$_4^-$),[13] **B** was synthesized by the reduction of MnO$_4^-$ by Cl$^-$ under strongly acidic conditions and in the absence of alkaline-earth cations. As found before, birnessites formed from MnO$_4^-$ reduction in the presence of K$^+$ as the main cationic species are materials with a much lower surface area of up to 50 m^2 g^{-1} versus ∼200 m^2 g^{-1} typically found for the products of the alkaline synthesis route when Ca^{2+} is added.[13] Therefore, the S_{BET} of 25 m^2 g^{-1} found for **B** is within the expected range for synthetic potassium birnessites. Despite its lower specific surface area, this material is still reasonably active, and as a result, the catalytic rate per surface area is the by far best observed here. Because the overall performance of the catalytic system seems to us (and others) of prime importance, we would still conclude that **T$_{400}$**, **B@MF**, and **B@MG** are the best catalytic materials of the presented comparison (Figure 7). Nevertheless, our results suggest that the "acid route" yielding birnessite **B** should be investigated further; if one succeeds to enhance the specific surface area of this material without affecting the high catalytic rate per square meter, a truly superior new catalyst could emerge.

A look at Table 2 or Figure 7 shows that the move from a "monolithic" manganese oxide material **B** to the core−shell architectures **B@FeO$_x$** has profound effects on the catalytic performance. This might be explained in at least three different ways.

First, the iron oxide cores could directly improve catalysis. It might be that it is beneficial to have an iron oxide core because the nanoscopic manganese oxide shell is thus effectively wired to an underlying, more conducting support. FeO$_x$ at the core should be a better hole conductor than MnO$_x$, so that the holes needed for the water oxidation process (four H$^+$ per formed oxygen) are more mobile in the material and thus able to accumulate faster at an active center in these materials. The magnetic core can also induce an interfacial polarization effect on the shell. This could well explain the observed higher catalytic activities of **B@MF** and **B@MG** in comparison to **B@MH** considering the higher conductivities of the pure **MG** and **MF** phases with respect to **MH**.[28] Finally, the core material might influence the organization of the shell, leading to distorted structures with differences in cation sites and Mn−Mn or Mn−O distances. As recently shown by Robinson et al.,[29] surface-active sites in manganese oxides are derived from underlying crystal structures. We obtained well-defined core−shell composites with spinel **MF** and **MG**. It appears that MnO$_x$ layers close to the core−shell interface perceive the structural characteristics of the iron oxide core and a thin shell imposed by the ordering effects of the core would therefore be more surface-active, corroborating the results shown in Figure 7. No such uniform coating and particle-size distribution could be obtained with **MH**, and rather big manganese oxide aggregates formed with embedded core particles (as also reported by Zhai et al.[19]).

A second possibility is the incorporation of a certain amount of iron into the birnessite structure during the preparation process, which would result in a different material, an "iron birnessite", and could thus explain the differences in the catalytic activity. We performed a XPS sputtering measurement to gain information about the depth profile of the core−shell composites. As shown in Figure 8, the manganese concentration diminishes through the depth while that of iron increases as a feature of the core−shell structure. However, the iron concentration seems to be around 5−10% before sputtering, suggesting that some iron does exist in the shell or its presence might possibly be due to destruction of the heterogeneous shell around the magnetic core during the sputtering process. Angle-resolved XPS assumes that homogeneous layers are present in the samples and can give erroneous data should the layers be heterogeneous.[30] Therefore, we refrain to absolutely define the shell as an iron birnessite, but this is clearly a possibility, as was already discussed above (see the elemental compositions in Table 1).

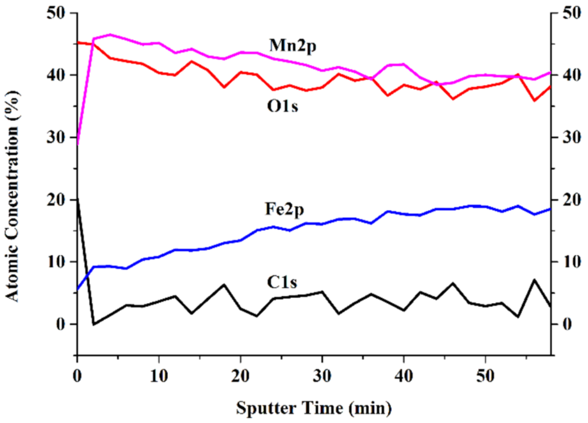

Figure 8. XPS depth profiles of C 1s, Fe 2p, O 1s, and Mn 2p for **B@MG** as a function of the sputtering time. Sample sputtering was performed for 30 cycles using 2 keV Ar^+ rastered over a 2 μm × 2 μm area of the specimen. The sputtering time for each cycle was 2 min.

As a third explanation, the architecture of the particles might be key. Not all manganese ions of the particles are part of the water oxidation active sites. For this last possibility, we introduce two models for the areas where water oxidation might occur in core−shell particles.

A birnessite is a manganese oxide consisting of layers of MnO_6 octahedra with water between the layers. In one possibility (Figure 9, "active zone model"), catalysis takes place only in the outermost part of the particles. With a hydration radius of at least 4.5 Å,[31] Ce^{4+} is most likely not able to enter deep into the materials and thus reacts only at the particles' outer surfaces. The resulting injected holes are able to migrate a certain distance into the particle. Here, they can react with water molecules both on the surface and between the birnessite layers, resulting in oxygen evolution and the addition of fresh water substrate from the bulk. In this view, the catalytically active centers are thus expected to be located only within a small zone at the surface. An observation supporting this view is the fact that the birnessites interlayer space detectable by XRD does not change after exposure of **B** to a Ce^{4+} solution for 1 h (see the SI, Figure S10).

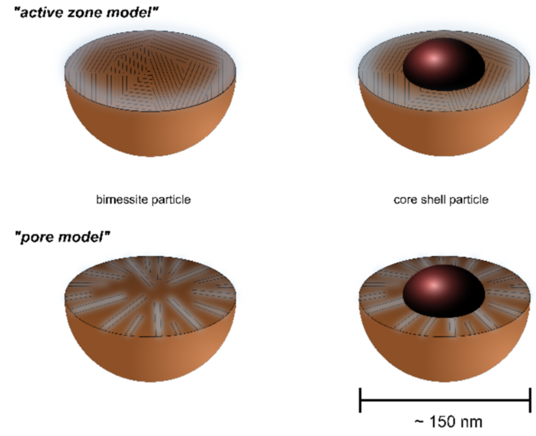

Figure 9. "Active zone model" and "pore model" for water oxidation at birnessite and core−shell composite particles.

Adsorption measurements and related studies on birnessites have indicated that birnessites are mesoporous materials.[32] In a "pore model" (Figure 9), we assume that these pores can be entered by Ce^{4+} and holes can be produced deep inside the particles on the inner walls of the pores. Water is also able to diffuse into these pores, and thus there should be accessible active sites in the entire birnessite volume.

We observed pronounced differences for the catalytic rates per BET surface area (Table 2 and Figure S9 in the SI) and therefore the size of the surface area accessible for N_2 adsorption alone seem not to be the predominant factor influencing the catalytic activity in the studied birnessite-based systems. Instead, our data suggest that if the morphology factors are important for catalytic rates, a much more detailed analysis will be needed, taking into account the scenarios shown in Figure 9. The relationship between the particle shape and catalysis can only be explained once a better understanding of the most likely very complex interactions and dynamics of water, protons, oxidation agent Ce^{4+}, and injected electron holes with respect to both the outer surfaces and the pores of the birnessite materials has been developed.

CONCLUSIONS

In this contribution, we report magnetic composite catalysts, which show promising catalytic rates for water oxidation. The catalysts were prepared by supporting a "birnessite-type" water oxidation catalyst on three types of nanosized iron oxides in a core−shell manner. Nearly spherical nanocomposite particles were obtained containing an iron oxide core of 50−60 nm diameter with a birnessite shell of 40−50 nm thickness, composed of curled nanosheets of 5 nm thickness. Chemical analysis results showed that the shell is mainly an acid birnessite, but XPS also indicated the possible incorporation of iron ions into the birnessite coating. Thus, the large potassium ions that are often intercalated between the manganese oxide layers were under our synthesis conditions (low pH and the presence of iron) expelled from the interlayer space probably because of geometric strain on the layers during the coating process.

Chemical water oxidation measurements were performed using Ce^{4+}, and a substantial increase in the catalytic activity per manganese (rates about 50% faster) or per gram (∼+15%) was detected when birnessite was supported on **MF** and **MG** cores. For the studied compounds, the composite catalyst **B@MF** displayed the highest catalytic activity per manganese basis (3150 mmol_{O_2} mol_{Mn}^{-1} h^{-1}), and this catalytic rate ranks among the fastest observed so far for MnO_x catalysts in reactions using the Ce^{4+} oxidant. This indicates a synergistic effect of the core and shell for the nanocomposites, which might be explained by the fact that the core either provides a more conducting medium or creates structural changes in the shell, resulting from interfacial ordering. Alternatively, the core might influence the composition, thickness, and surface properties of the shell, and morphology factors could dominate. All of these effects, and also others not yet hypothesized, are impossible to separate so far. From comparisons of the catalytic rates and particle morphologies, we propose a model where the catalytically active and accessible manganese centers are most likely present not just at the outer particle surfaces but also in a significantly extended "active zone" and pores, thus creating catalytically active interfaces deep within the particles.

On a per manganese or per mass basis, the magnetic core−shell catalysts catalyze water oxidation as efficiently as optimized calcium birnessite catalysts (fastest detected rates: ∼3000 mmol_{O_2} mol_{Mn}^{-1} h^{-1}), which up to now performs best among manganese oxides in Ce^{4+} experiments.[8,11−13] Although such catalyst screenings are limited because of the well-known drawbacks of using the sacrificial agent Ce^{4+}, this new composite system appears to have a potential toward higher catalytic activities with tuning options of the core−shell structure and surface chemistry. The possibility of practical recovery by an external magnetic field could be important for potential utilization in industrial applications. Additionally, the incorporation of appropriate iron oxides can lead to an increase of the charge carrier mobility, an important property once the materials are used as electrocatalysts for water-oxidizing anodes. Finally, the spherical shape would be another advantage in packing the catalyst to an appropriately designed reactor, resulting in maximum exposure of the catalyst surface to the working solution.

We conclude that these newly designed magnetic core−shell catalysts offer a promising novel concept for water oxidation reactions. The properties of the nanocomposites have to be analyzed in more detail to understand the decisive factors for efficient catalysis. Additionally, research is underway toward optimization of the core−shell parameters to obtain new compositions also using different types of manganese oxide shells.

■ ASSOCIATED CONTENT

Ⓢ Supporting Information

SEM images of **MH** and **MG**, SEM−EDS maps of **B@MH** and **B@MG**, TEM images of **MH**, **MG**, **B@MH**, and **B@MG**, SAED pattern for **B@MH**, TGA curves of **MF**, **MG**, and **MH**, room temperature magnetization curves of **B@MG** and **B@MH**, oxygen evolution curves normalized per catalyst mass, comparison of water oxidation rates per catalyst mass and surface area, illumination experiments, and comparison of XRD patterns of **B** before and after catalysis. This material is available free of charge via the Internet at http://pubs.acs.org.

■ AUTHOR INFORMATION

Corresponding Authors

*E-mail: philipp.kurz@ac.uni-freiburg.de. Phone: +49 761 2036127.
* E-mail: bkaran@hacettepe.edu.tr. Phone: +90 312 2977951.

Notes

The authors declare no competing financial interest.

■ ACKNOWLEDGMENTS

This work was supported by the Scientific and Technological Research Council of Turkey (Project 113Z009). G.E. and P.K. acknowledge the EU Erasmus Programme for financing visits to Freiburg and Ankara, respectively. The authors thank UNAM Laboratories, Bilkent University for TEM imaging, the METU Central Laboratory for surface and XPS analyses, and the Hacettepe University Physics Engineering Department for magnetic measurements. Work in Freiburg was made possible by financial support of the Deutsche Forschungsgemeinschaft (Project KU 2885/1-1).

■ REFERENCES

(1) Barber, J. *Chem. Soc. Rev.* **2009**, *38*, 185−196.
(2) Ferreira, K. N.; Iverson, T. M.; Maghlaoui, K.; Barber, J.; Iwata, S. *Science* **2004**, *303*, 1831−1838.
(3) Cady, C. W.; Crabtree, R. H.; Brudvig, G. W. *Coord. Chem. Rev.* **2008**, *252*, 444−455.
(4) Mullins, C. S.; Pecoraro, V. L. *Coord. Chem. Rev.* **2008**, *252*, 416−443.
(5) Najafpour, M. M. Manganese compounds as water oxidizing catalysts in artificial photosynthesis. *Artificial Photosynthesis*; InTech: Rijeka, Croatia, 2012; pp 37−52.
(6) Yagi, M.; Narita, K.; Maruyama, S.; Sone, K.; Kuwabara, T.; Shimizu, K. *Biochim. Biophys. Acta, Bioenerg.* **2007**, *1767*, 660−665.
(7) Dismukes, G. C.; Brimblecombe, R.; Felton, G. A. N.; Pryadun, R. S.; Sheats, J. E.; Spiccia, L.; Swiegers, G. F. *Acc. Chem. Res.* **2009**, *42*, 1935−1943.
(8) Berends, H. M.; Homburg, T.; Kunz, I.; Kurz, P. *Appl. Clay Sci.* **2011**, *53*, 174−180.
(9) Harriman, A.; Pickering, I. J.; Thomas, J. M.; Christensen, P. A. *J. Chem. Soc., Faraday Trans.* **1988**, *1*, 2795−2806.
(10) Luneva, N. P.; Shafirovich, V. Y.; Shilov, A. E. *J. Mol. Catal.* **1989**, *52*, 49−62.
(11) Najafpour, M. M.; Ehrenberg, T.; Wiechen, M.; Kurz, P. *Angew. Chem., Int. Ed.* **2010**, *49*, 2233−2237.
(12) Wiechen, M.; Zaharieva, I.; Dau, H.; Kurz, P. *Chem. Sci.* **2012**, *3*, 2330−2339.
(13) Frey, C.; Wiechen, M.; Kurz, P. *Dalton Trans.* **2014**, *43*, 4370−4379.
(14) Zaharieva, I.; Najafpour, M. M.; Wiechen, M.; Haumann, M.; Kurz, P.; Dau, H. *Energy Environ. Sci.* **2011**, *4*, 2400−2408.
(15) Wiechen, M.; Berends, H. M.; Kurz, P. *Dalton Trans.* **2012**, *41*, 21−31.
(16) Hocking, R. K.; Brimblecombe, R.; Chang, L. Y.; Singh, A.; Cheah, M. H.; Glover, C.; Casey, W. H.; Spiccia, L. *Nat. Chem.* **2011**, *3*, 461−466.
(17) Ahmed, K. A. M.; Huang, K. *Mater. Chem. Phys.* **2012**, *133*, 605−610.
(18) Najafpour, M. M.; Rahimi, F.; Aro, E. M.; Lee, C. H.; Allakhverdiev, S. I. *J. R. Soc., Interface* **2012**, *9*, 2383−2395.
(19) Zhai, Y.; Zhai, J.; Zhou, M.; Dong, S. *J. Mater. Chem.* **2009**, *19*, 7030−7035.
(20) Zhu, H. T.; Luo, J.; Yang, H. X.; Liang, J. K.; Rao, G. H.; Li, J. B.; Du, Z. M. *J. Phys. Chem. C* **2008**, *112*, 17089−17094.
(21) McKenzie, R. M. *Mineral. Mag.* **1971**, *38*, 493−502.
(22) Devaraj, S.; Munichandraiah, N. *J. Phys. Chem. C* **2008**, *112*, 4406−4417.
(23) Johnson, E. A.; Post, J. E. *Am. Mineral.* **2006**, *91*, 609−618.
(24) Lu, H. M.; Zheng, W. T.; Jiang, Q. *J. Phys. D: Appl. Phys.* **2007**, *40*, 320−325.
(25) Iyer, A.; Del-Pilar, J.; King'ondu, C. K.; Kissel, E.; Garces, H. F.; Huang, H.; El-Sawy, A. M.; Dutta, P. K.; Suib, S. L. *J. Phys. Chem. C* **2012**, *116*, 6474−6483.
(26) Shevela, D.; Koroidov, S.; Najafpour, M. M.; Messinger, J.; Kurz, P. *Chem.—Eur. J.* **2011**, *17*, 5415−5423.
(27) Sivula, K.; Le Formal, F.; Grätzel, M. *ChemSusChem* **2011**, *4*, 432−449.
(28) Iwauchi, K. *Jpn. J. Appl. Phys.* **1971**, *10*, 1520−1528.
(29) Robinson, D. M.; Go, Y. B.; Mui, M.; Gardner, G.; Zhang, Z.; Mastrogiovanni, D.; Garfunkel, E.; Li, J.; Greenblatt, M.; Dismukes, G. C. *J. Am. Chem. Soc.* **2013**, *135*, 3494−3501.
(30) Openstax Home Page: http://cnx.org/content/m34527/1.1/ (accessed Sept 12, 2014).
(31) Lutz, O. M. D.; Hofer, T. S.; Randolf, B. R.; Weiss, A. K. H.; Rode, B. M. *Inorg. Chem.* **2012**, *51*, 6746−6752.
(32) Gorlin, Y.; Lassalle-Kaiser, B.; Benck, J. D.; Gul, S.; Webb, S. M.; Yachandra, V. K.; Yano, J.; Jaramillo, T. F. *J. Am. Chem. Soc.* **2013**, *135*, 8525−8534.